Carrier-Type Modulation and Mobility Improvement of Thin MoTe$_2$

Deshun Qu, Xiaochi Liu, Ming Huang, Changmin Lee, Faisal Ahmed, Hyoungsub Kim, Rodney S. Ruoff, James Hone, and Won Jong Yoo*

A systematic modulation of the carrier type in molybdenum ditelluride (MoTe$_2$) field-effect transistors (FETs) is described, through rapid thermal annealing (RTA) under a controlled O$_2$ environment (p-type modulation) and benzyl viologen (BV) doping (n-type modulation). Al$_2$O$_3$ capping is then introduced to improve the carrier mobilities and device stability. MoTe$_2$ is found to be ultrasensitive to O$_2$ at elevated temperatures (250 °C). Charge carriers of MoTe$_2$ flakes annealed via RTA at various vacuum levels are tuned between predominantly pristine n-type ambipolar, symmetric ambipolar, unipolar p-type, and degenerate-like p-type. Changes in the MoTe$_2$-transistor performance are confirmed to originate from the physical and chemical absorption and dissociation of O$_2$, especially at tellurium vacancy sites. The electron branch is modulated by varying the BV dopant concentrations and annealing conditions. Unipolar n-type MoTe$_2$ FETs with a high on–off ratio exceeding 10^6 are achieved under optimized doping conditions. By introducing Al$_2$O$_3$ capping, carrier field effect mobilities (41 for holes and 80 cm^2 V^{-1} s^{-1} for electrons) and device stability are improved due to the reduced trap densities and isolation from ambient air. Lateral MoTe$_2$ p–n diodes with an ideality factor of 1.2 are fabricated using the p- and n-type doping technique to test the superb potential of the doping method in functional electronic device applications.

The family of two-dimensional (2D) layered materials has expanded rapidly since the discovery of graphene in 2004.[1] Among the 2D semiconductors, molybdenum disulfide (MoS$_2$), tungsten diselenide (WSe$_2$), and black phosphorus (BP) have been intensively studied for use in field effect transistors (FETs), tunnel field effect transistors (TFETs), optoelectronic devices, and complementary metal-oxide-semiconductor transistors (CMOS).[2–8] The fabrication of unipolar p-type and n-type FETs with controllable carrier concentrations is of fundamental importance for the realization of a variety of functional electronic devices, including TFETs, CMOS, and p–n junctions. MoS$_2$ FETs have been praised for their low off-current and high electron mobility,[2,9] which are favorable features in electronic switches; however, p-type MoS$_2$ FETs are seldom achieved due to the strong pinning effect at the metal–MoS$_2$ interface,[10] which impedes their use in CMOS electronics and p–n junctions. The MoS$_2$

D. Qu, X. Liu, Prof. W. J. Yoo
Samsung-SKKU Graphene/2D Center (SSGC)
Department of Nano Science and Technology
SKKU Advanced Institute of Nano-Technology (SAINT)
Sungkyunkwan University
2066 Seobu-ro, Jangan-gu, Suwon
Gyeonggi-do 16419, Republic of Korea
E-mail: yoowj@skku.edu
M. Huang, Prof. R. S. Ruoff
Center for Multidimensional Carbon Materials (CMCM)
Institute for Basic Science (IBS)
Ulsan 44919, Republic of Korea
M. Huang, Prof. R. S. Ruoff
School of Materials Science and Engineering
Ulsan National Institute of Science and Technology (UNIST)
Ulsan 44919, Republic of Korea
C. Lee, Prof. H. Kim
School of Advanced Materials Science and Engineering
Sungkyunkwan University
2066 Seobu-ro, Jangan-gu, Suwon
Gyeonggi-do 16419, Republic of Korea

F. Ahmed, Prof. W. J. Yoo
School of Mechanical Engineering
Sungkyunkwan University
2066 Seobu-ro, Jangan-gu, Suwon
Gyeonggi-do 16419, Republic of Korea
Prof. R. S. Ruoff
Department of Chemistry
Ulsan National Institute of Science and Technology (UNIST)
Ulsan 44919, Republic of Korea
Prof. J. Hone
Department of Mechanical Engineering
Columbia University
New York, NY 10027, USA

The ORCID identification number(s) for the author(s) of this article can be found under https://doi.org/10.1002/adma.201606433.

bandgap falls in the range 1.8–1.3 eV, for monolayer and bulk MoS_2, which is undesirable for driving high currents in TFETs. Despite the accessibility to both electron and hole conduction in WSe_2,[5,11] the WSe_2 bandgap is similar to that of MoS_2; thus, high-performance TFETs cannot be prepared using WSe_2. BP is predicted to be a promising material for TFET application due to its favorable small bandgap of 0.3 eV in the bulk state;[12] however, BP is usually hole-doped,[13] and researchers must continue to seek methods of effectively modulating its carrier type[14–16] to realize homogeneous BP TFETs.

2H-type molybdenum ditelluride ($MoTe_2$), a 2D layered semiconductor, has recently gained attention for its potential utility in TFETs.[17] Few-layer $MoTe_2$ has a small indirect bandgap of 0.9 eV,[18–20] rendering it promising for realizing TFETs with high tunneling current. This small bandgap also extends the operating range of transition metal dichalcogenide (TMD) optoelectronic devices from the visible to the near-infrared.[19] Intrinsic $MoTe_2$ transistors display ambipolar transfer characteristics, demonstrating that the pinning effects in metal–$MoTe_2$ contacts are relatively weak[21,22] compared to contacts between metals and sulfur-terminated TMDs[23,24] or BP.[25] Unipolar conduction of electrons and holes in $MoTe_2$ may potentially be possible simply through work function engineering of contact metal. The high work function of Pt and the low work function of Ti contacts have been reported to strengthen the p- and n-branches, respectively; however, such devices were p- or n-dominated and were ambipolar.[21] CMOS built with ambipolar transistor cannot surpass the current technology where both p-type and n-type transistors are used because the integration of the two shows better performance and lower power consumption. TFETs also require unipolar p- and n-type $MoTe_2$ FETs of high carrier concentrations. Unipolar p-type behavior has been observed in chemical vapor deposited (CVD) $MoTe_2$ flakes with Ti/Au contacts,[26] and oxygen present in the environment can tune the device properties from ambipolar to unipolar p-type.[27] These processes, however, are not typically well-controlled, and the properties of $MoTe_2$ FETs cannot generally be designed to meet the requirements of various electronic or optical devices. The field effect mobilities reported for these ambipolar or unipolar p-type devices fall in the range 0.3–20 $cm^2 V^{-1} s^{-1}$ for holes and 0.03–30 $cm^2 V^{-1} s^{-1}$ for electrons.[18,22,28] Effective and controllable doping methods that modulate the carrier type and permit mobility improvement of $MoTe_2$ FETs must be developed to enable applications in a variety of functional devices. We should know all semiconducting TMDs are capable of showing ambipolar conduction under sufficient gate modulation independently to the inherent doping level of the flake.[18,29,30] The polarities of TMDs transistors we referred to are based on low-k gate dielectrics (such as SiO_2), in which case the gate capacitance is too low to shift the chemical potential across the gap when the crystals are highly doped or to fully develop ambipolar transport. In other words, the controlled doping of $MoTe_2$ is only relevant if actual applications are based on FETs with low-k gate dielectrics.

Here, unipolar p- and n-type $MoTe_2$ FETs with on–off current ratios of 10^5 and 10^6 were prepared through rapid thermal annealing (RTA) and benzyl viologen (BV) doping, respectively. By varying the vacuum level in the RTA chamber prior to annealing and the BV dopant concentration, annealing conditions, hole and electron doping concentrations could be modulated over a wide range, from slight doping to degenerate-like doping. Al_2O_3 was then deposited onto the pristine ambipolar device and annealed p-type device for mobility improvement. Surprisingly, a unipolar n-type device with enhanced electron current and almost negligible hysteresis could be prepared. The electron field effect mobility was improved to 80 from 5 $cm^2 V^{-1} s^{-1}$ in the pristine device. The hole mobility of the annealed p-type device increased to 41 $cm^2 V^{-1} s^{-1}$ and the hysteresis was also reduced. The Al_2O_3-capped devices exhibited excellent stability in both ambient air and under vacuum conditions, compared to the un-capped devices, which tended to oxidize easily in air. Finally, we fabricated a lateral homogeneous $MoTe_2$ p–n diode that combined electron and hole doping techniques. The device displayed superior diode properties with a high rectification ratio of 10^4 at 0 gate bias, as well as an ideality factor of 1.2.

The device fabrication process is described in detail in the Experimental Section. We characterized the as-prepared pristine $MoTe_2$ FET performances, as shown in **Figure 1**. The transfer
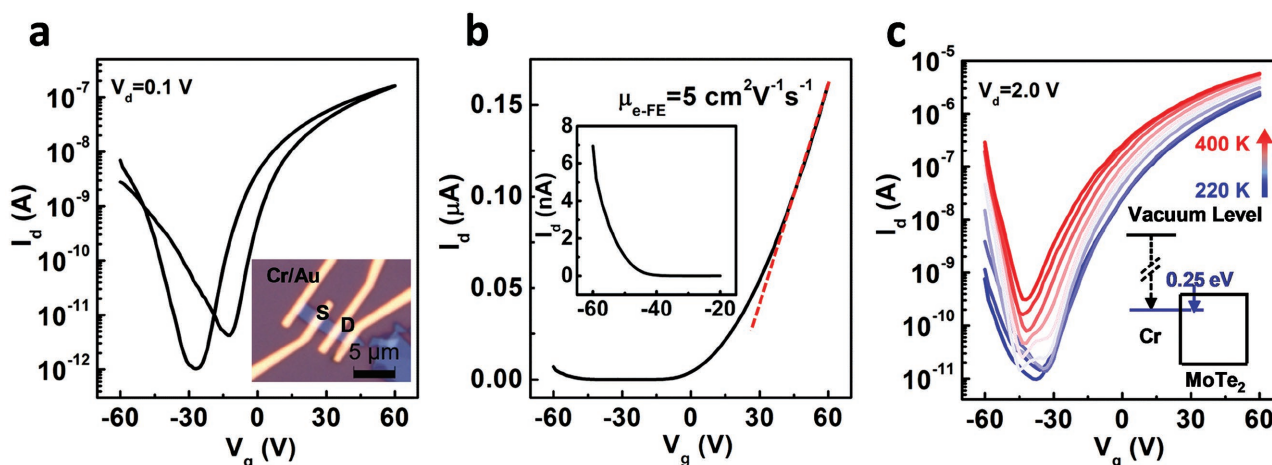

Figure 1. Electrical performance of a pristine $MoTe_2$ FET. a) Transfer characteristics of an as-prepared $MoTe_2$ FET. An optical microscopy image of the device is shown in the inset. b) Electron field effect mobility extraction from the linear plot of transfer curve, linear plot of hole branch is shown in the inset. c) Temperature dependence of the transfer characteristics, band alignment of Cr–$MoTe_2$ contact is shown in the inset.

**ADVANCED
SCIENCE NEWS**

www.advancedsciencenews.com

**ADVANCED
MATERIALS**

www.advmat.de

characteristics at a drain bias of 0.1 V are shown in Figure 1a, and an optical microscopy image of the device is shown in the inset. The transfer curve was obtained at the middle two electrodes of the four-probe device, with a channel length and width of 1.4 and 1.8 μm, respectively. The flake thickness was confirmed to be 11 nm by atomic force microscopy, as shown in Figure S1a in the Supporting Information. (All flakes used in this work were 8–15 nm thick.) Pristine $MoTe_2$ transistors with Cr/Au contacts displayed ambipolar transfer characteristics. The electron current was almost two orders of magnitude higher than the hole current. A large hysteresis was observed in the transfer curve, indicating a non-negligible trap state density at the flake surface or the $MoTe_2$–SiO_2 interface. The electron field effect mobility was calculated to be 5 cm^2 V^{-1} s^{-1} from a four-probe measurement[31] with $\mu_{FE} = \dfrac{L}{W} \dfrac{dI_d}{C_g V_d dV_g}$, where L and W are the length and width of the sample, C_g is the capacitance per unit area of the corresponding dielectric layer. For four-probe measurement, V_d is the voltage drop at the middle two electrodes and thus contact resistance is excluded. We extracted dI_d/dV_g from the linear regime of I_d–V_g plot as shown in Figure 1b. A linear plot of the p-branch is shown in the inset of Figure 1b, it is operated in the sub-threshold regime even under $V_g = -60$ V, showing an extremely low hole density in the pristine device. Electron density is also low according to our calculation on channel sheet resistance and contact resistance based on four-probe measurement. Detailed discussion on the contribution from each resistance to the total resistance, which determines the device current, is described in Figure S1 in the Supporting Information. In general, gate modulation is not sufficient to induce high electron density in $MoTe_2$ FETs. The channel resistance remained high for electrons at $V_g = 60$ V, and thus limited the on-current density of the n-branch. Hole density is even lower since the chemical potential of the pristine device located in the upper band of $MoTe_2$. The above conclusion can be proved by the band alignment between Cr and $MoTe_2$, which was figured out by temperature-dependent measurements. The transfer curves at different temperatures are plotted in Figure 1c. Both the electron and hole currents increased with the temperature. The temperature dependence of the electron current agreed well with the thermionic emission (Figure S2, Supporting Information), whereas the hole current should be interpreted as arising from a thermal-assisted tunneling process.[21] The flat band Schottky barrier height (SBH) was calculated to be 0.25 eV, the corresponding band alignment of Cr–$MoTe_2$ contact is shown in the inset of Figure 1c. Chemical potential of $MoTe_2$ lies close to the conduction band at flat band gate bias, higher negative gate voltage is not able to sufficiently shift down the chemical potential to achieve high hole current. Electron current is also limited under high positive gate bias. So, it is necessary to modulate the chemical potential of $MoTe_2$ flake through chemical doping, and thus unipolar $MoTe_2$ FETs with high current levels can be possibly achieved.

An appropriate chemical dopant can selectively tune the ambipolar transistor and provide a unipolar transistor with pronounced p- or n-channel behavior. $MoTe_2$ may be oxidized to form a p-doped material upon exposure to ambient conditions over time;[27] however, the p-doping process is time-consuming and uncontrolled, and the underlying mechanism is not well understood. Here, we developed an RTA doping process that tuned the performances of $MoTe_2$ transistors by varying the vacuum level in the RTA chamber before annealing and, therefore, precisely controlling the p-doping concentration. Differences in the O_2 concentrations at each vacuum level affected the doping results. The gradually changing transfer characteristics of the devices annealed at various vacuum levels are shown in **Figure 2**a. The performance of a pristine $MoTe_2$ device is displayed for reference. Prior to annealing, the RTA chamber was pumped down to 4, 8, and 40 mTorr, corresponding to the purple, red, and blue transfer curves of the annealed devices, respectively. The annealing process was carried out at 250 °C and lasted for 3 h in the RTA chamber. After annealing under a 4 mTorr atmosphere, the transfer curve of the $MoTe_2$ device approached that of a symmetric ambipolar device with a slightly higher electron current level compared to the hole current level. The conductivity minimum point[32] shifted by 25 V toward positive values compared to the pristine device, and the hole current increased by more than two orders of magnitude. As the vacuum pressure was increased to 8 mTorr, the transfer curve of the annealed device became unipolar p-type with an on–off ratio of up to 10^5. The off-current of the annealed unipolar p-type device was found to be as low as that of a pristine device, whereas the hole on-current increased by almost three orders of magnitude, reaching a current level comparable to the electron current of the pristine device. Comparable electron and hole branch performances indicated that $MoTe_2$ is suitable for fabricating complementary devices. We noticed that the conductivity minimum point of the annealed unipolar p-type device shifted to nearly 60 V, indicating a high doping level after the annealing process. The $MoTe_2$ device annealed under a 40 mTorr atmosphere revealed degenerate-like transfer characteristics with an on–off ratio of less than 10 (blue curve), indicating a further downshift in the chemical potential toward the valence band. The sheet density of holes in the unipolar p-type device was calculated as $n_{2D} = C_g(V_g - V_{th})/e$.[33] Here C_g is the gate oxide capacitance per unit area, V_g is the gate voltage, V_{th} is the threshold voltage, and e is the electron charge. The maximum hole density reached 5 × 10^{12} cm^{-2} at a –60 V gate bias. The hole field effect mobility of the doped unipolar p-type device was calculated to be 21 cm^2 V^{-1} s^{-1} from measurements collected in the four-probe configuration (Figure 2b). This value is comparable to the highest hole mobilities ever obtained at room temperature.[34,35] The output curves of the doped unipolar p-type device are much more linear and symmetric than the p-branch of the pristine device (Figure 2b inset), showing good contact properties.

The polar transition mechanism in the $MoTe_2$ device after annealing was examined by measuring the temperature-dependent characteristics of the doped ambipolar device. The results are shown in Figure 2c. Within the temperature range, the electron branch displayed a temperature dependence trend similar to that of the pristine device, although less pronounced. By contrast, the hole branch behaved almost independently of the temperature, revealing tunneling-dominated contact properties. The temperature dependence of the doped device revealed a higher Schottky barrier for electrons and a high but much thinner Schottky barrier for holes after annealing. These
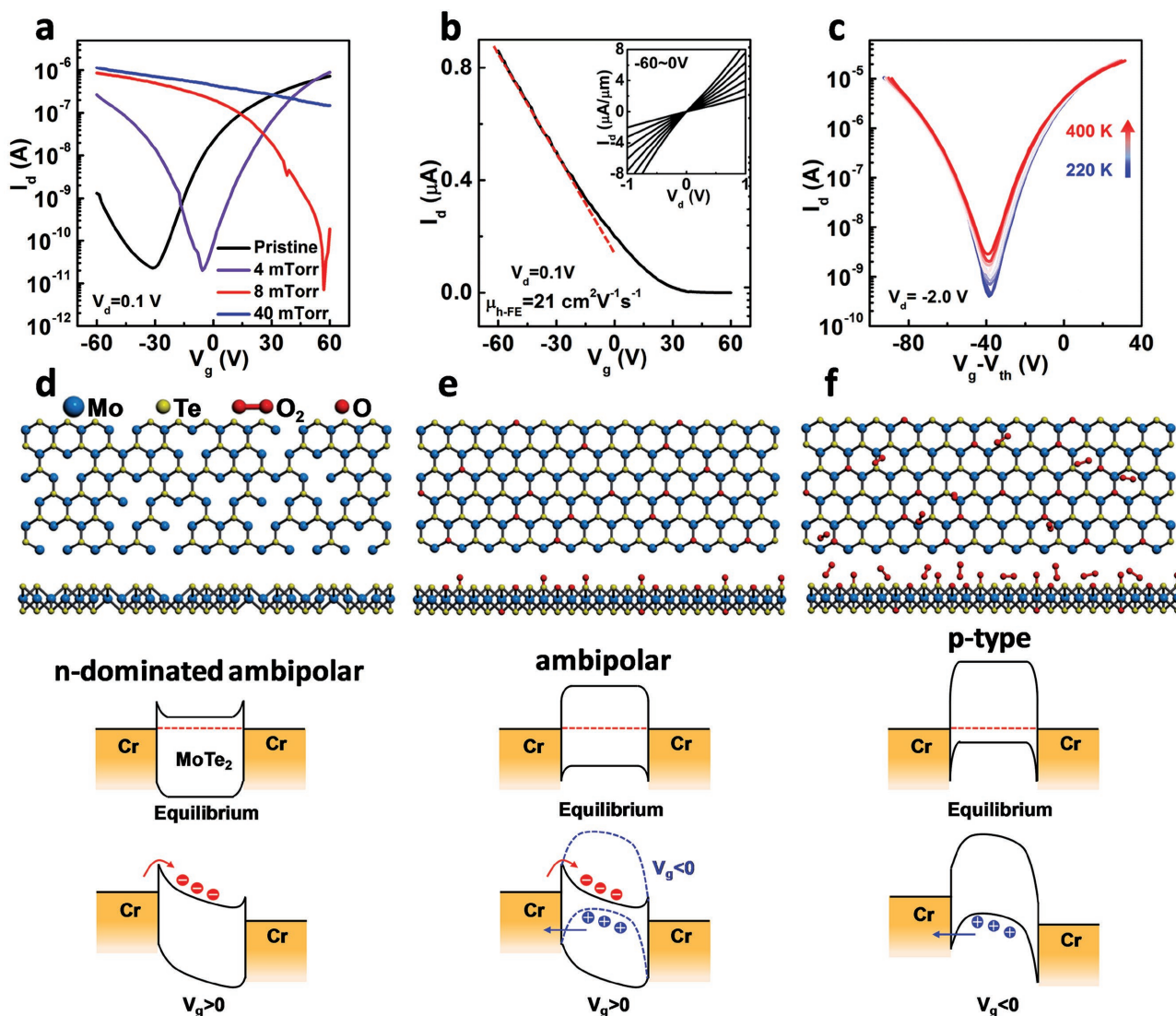
Figure 2. p-Type doping induced by annealing. a) Transfer characteristics of the devices annealed in an RTA chamber at different vacuum levels. b) Hole mobility calculated from the unipolar p-type MoTe$_2$ transistor, output curves are shown in the inset. c) Temperature-dependent transfer curves obtained from a doped ambipolar device. The top panels of (d–f) show the top (upper) and side views (lower) of the atomic configurations of the MoTe$_2$ flakes in a pristine n-dominated ambipolar device, an RTA-treated symmetric ambipolar device, and an RTA-treated unipolar p-type device, respectively. The corresponding band diagrams are shown in the bottom panels.

results could be explained in terms of the chemical potential shift in MoTe$_2$, as discussed below.

The mechanism by which the doping levels was varied during annealing could be explained by inspection of the top (upper) and side views (lower) of the atomic configurations, as shown in the top panels of Figure 2d–f, respectively. Band diagrams illustrating the carrier transport paths corresponding to each doping level are displayed in the bottom panels. Monolayer or few-layer MoTe$_2$ fabricated from both micromechanical cleavage and CVD methods always contain some stable defects, such as tellurium vacancies. Single tellurium vacancies can be formed under electron beam irradiation. The atomic configurations of a pristine MoTe$_2$ flake with single tellurium vacancies are shown in the top panel of Figure 2d. The missing tellurium atoms created energy states within the

band gap close to the conduction band, which induced Fermi level pinning around the defect levels. Band diagrams of Cr in contact with a pristine MoTe$_2$ flake are shown in the bottom panel of Figure 2d. O$_2$ molecules tend to chemically adsorb onto tellurium defect sites and then dissociate into two oxygen atoms.[36] One oxygen atom replaces the tellurium vacancy and saturates the dangling bond whereas the other oxygen atom either remains stationary or diffuses to a nearby region of the MoTe$_2$ sheet, as shown in the top panel of Figure 2e. The absorption of an oxygen molecule can completely remove the defect states in the gap region due to the saturation effect caused by the formation of Mo−O bonds at the vacancy sites. Both the chemical absorption and dissociation processes must overcome certain energy barriers. Annealing the sample at 250 °C promotes the chemical absorption and dissociation of

O_2 molecules at vacancy sites. Because the O_2 concentration was limited under a 4 mTorr atmosphere, O_2 molecules preferably interacted with dangling bonds at the vacancy sites and inhibiting further absorption of O_2 molecule at other sites. After compensating for the defect energy levels in the gap region, the chemical potential of the repaired flake moved toward the middle of the $MoTe_2$ bandgap. The equilibrium band alignment of Cr and the annealed $MoTe_2$ is illustrated in the bottom panel of Figure 2e, corresponding to the symmetric ambipolar transfer characteristics of the device. At equilibrium state, the upward band bending increases the effective SBH of electrons. Application of a small positive gate bias did not significantly change the SBH. The high SBH blocked electron emission over it, resulting in a low electron current and weak temperature dependence, as described in Figure 2c. At a high positive gate bias, the effective SBH decreased to a height similar to that of the pristine device. Electron current in the annealed device was as high as that of the pristine device. The effective SBH for the hole branch was lower than that in the pristine device after annealing, but the barrier height remained too high for hole emission; therefore, only tunneling could take place. Application of a negative gate bias thinned the barrier to facilitate hole tunneling through the barrier, leading to a high hole current level. Noted that hole transport in the pristine device was also interpreted as tunneling, although it strongly depended on the temperature, whereas almost no temperature dependence was observed in the doped device. The presence of gap states traps the holes in pristine device; thus, the tunneling process is temperature-dependent. After annealing, the gap states are eliminated by terminal oxygen groups on the dangling bonds of the tellurium vacancies, rendering the tunneling process temperature-independent while also enhancing the mobility. As the O_2 concentration was further increased (under a vacuum level of 8, 40 mTorr), additional physical and chemical absorption occurred across the $MoTe_2$ sheet, as illustrated in the top panel of Figure 2f. The absorbed O_2 molecules acted as electron acceptors to gain electrons from the $MoTe_2$ flake.[27,36,37] The $MoTe_2$ devices annealed at higher pressures were turned into unipolar p-type devices, as indicated by the band diagram in the bottom panel of Figure 2f.

To confirm and understand the doping mechanism, X-ray photoelectron spectroscopy (XPS) characterization was carried out on $MoTe_2$ samples of pristine condition and annealed in RTA chamber of varied vacuum levels. All spectra were calibrated using the C 1s peak at 284.6 eV as a reference. Binding energy (BE) shifts in XPS spectra for core level electrons have been used to identify the doping type in MoS_2.[38–40] Here, we also compared the BEs for Mo 3d and Te 3d peaks of the pristine $MoTe_2$ and thermal treated $MoTe_2$ samples. As shown in **Figure 3**a,b, both Mo 3d and Te 3d peaks shift by ≈0.1 and 0.4 eV to lower BEs for the $MoTe_2$ treated at 4 and 40 mTorr, respectively. Because the BEs of XPS spectra is referred to chemical potential in the materials, the downward shifts of binding energy can be interpreted by the move down of the chemical potential in the semiconductor. This result indicates the p-doping of the $MoTe_2$ after thermal treatment at 250 °C, especially at 40 mTorr. The presence of Te vacancies in the pristine $MoTe_2$ could also be confirmed by the atomic ratios of Te/Mo (around 1.90) acquired from the XPS spectra. After thermal treatment, the atomic ratios of Te/Mo ranges from 1.88–1.94, suggesting that there was no obvious change of the stoichiometric value for $MoTe_2$. As we observed p-doping in the thermal treated $MoTe_2$ samples, we further checked the XPS of Mo 3p peak. The results are shown in Figure 3c. The binding energies of Mo $3p_{3/2}$ (394.0 eV) and Mo $3p_{1/2}$ (411.5 eV) correspond to the Mo 3p peaks of $MoTe_2$ bulk crystals. While the new peaks appeared at 397.7 and 415.3 eV represent the Mo^{6+} $3p_{3/2}$ and $3p_{1/2}$ doublets of MoO_3 or MoO_x suboxides.[41] This result further indicates that O_2 could interact at the Te-vacancy sites to form Mo−O bond, thus resulting in the p-doping of the $MoTe_2$. The intensity of the new peaks increases with annealing pressure, which is consistent to our expectation. Since our annealing was carried out in a vacuum condition which contains limited O_2 and H_2O, the oxidation is controllable and mild. And thus, the observed intensity of the oxidation peaks is relatively small. Unlike MoS_2, $MoTe_2$ is more sensitive to doping process (hard
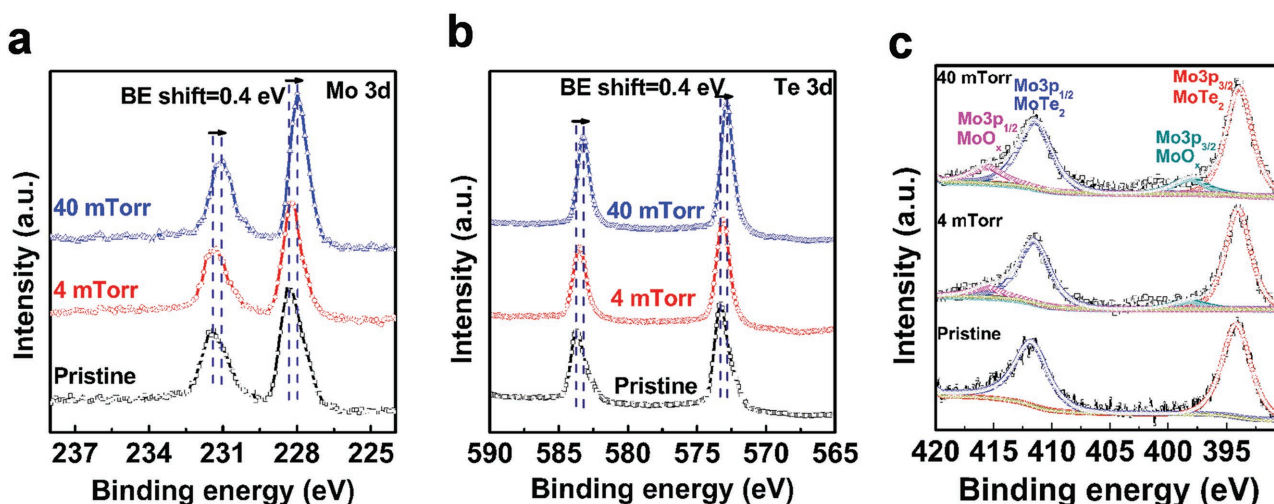
Figure 3. X-ray photoelectron spectroscopy characterization of p-type doping. The XPS core level spectra of a) Mo 3d, b) Te 3d, and c) Mo 3p in $MoTe_2$ samples under different annealing pressures.
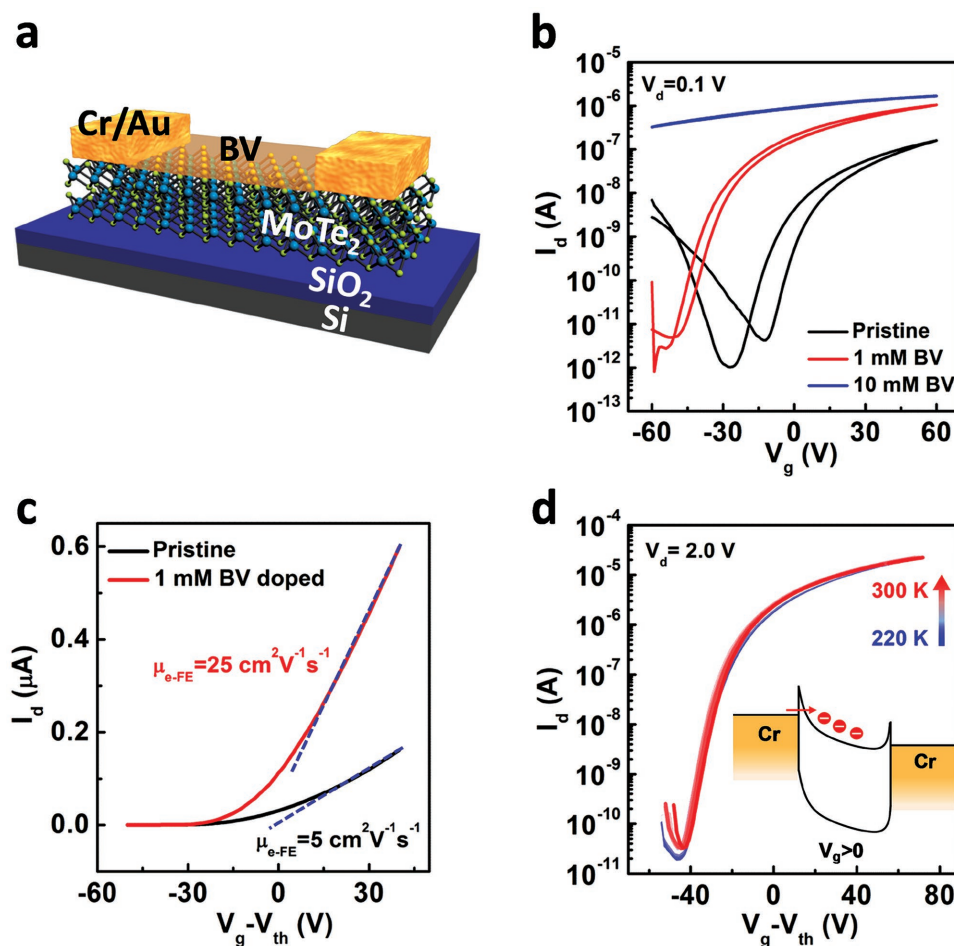
**ADVANCED
SCIENCE NEWS**

www.advancedsciencenews.com

**ADVANCED
MATERIALS**

www.advmat.de

Figure 4. n-Type doping with BV. a) Schematic diagram of the BV doping process. b) Transfer curves obtained from $MoTe_2$ transistors doped with 1×10^{-3} M (red curve) and 10×10^{-3} M (blue curve) BV dopant without annealing. The performance of a pristine device (black curve) is shown here for reference. c) Linear plot of transfer characteristics from the pristine device and the device after 1×10^{-3} M BV doping; Field effect mobilities of the devices were extracted from the linear regime of the transfer curves. d) Temperature-dependent transfer characteristics of a doped unipolar n-type $MoTe_2$ transistor. The band diagram in the inset illustrates electron transport through tunneling at the Cr–$MoTe_2$ interface after BV doping.

to control the doping concentration), so our well controlled mild doping process is of significant importance for developing high performance p-type $MoTe_2$ devices.

The n-branch of the $MoTe_2$ transistor was enhanced by applying the n-type dopant BV to $MoTe_2$. **Figure 4**a shows a schematic diagram of the BV doping process, the detailed operation of which is described in the Experimental Section. BV was used previously to achieve n-type charge transfer doping of MoS_2. Doped MoS_2 displayed an ultrahigh electron concentration with degenerate-like transfer characteristics.[42] We tested BV doping on $MoTe_2$; similarly, the doping always led to a high carrier density, even at a low dopant concentration of 1×10^{-3} M, if the annealing process was applied after spin coating, as it was for MoS_2 doping. These results are presented in Figure S4a in the Supporting Information. We then carried out the doping process without annealing; 10×10^{-3} M BV doping still resulted in degenerate transfer characteristics, whereas 1×10^{-3} M BV doping preserved the low off-current of the pristine $MoTe_2$ transistor but enhanced the on-current density by almost one order of magnitude, as shown in Figure 4b. (The device

presented in Figure 1 was doped.) The conductivity minimum point of the 1×10^{-3} M BV-doped device shifted to nearly −60 V; thus, the doped transistor was unipolar n-type with an on–off ratio of 10^6. Surprisingly, the hysteresis of the doped device was reduced. These results distinguish BV doping from other doping processes, such as plasma doping, which usually introduces defects or traps onto the surfaces of the flake, thereby aggravating the hysteresis and reducing the carrier mobility.[43] By contrast, electrons from the BV dopant neutralized the positively charged traps on the SiO_2 surface created during the thermal oxidation process, thereby providing a trap-free surface for electron transport. As a result, the electron mobility in the doped device was improved. We compared the electron field effect mobilities before and after BV doping under same $(V_g − V_{th})$, mobility of 1×10^{-3} M BV doped device was improved to 25 cm^2 V^{-1} s^{-1} compared to pristine 5 cm^2 V^{-1} s^{-1} as indicated in Figure 4c. The electron sheet density was improved to 5.2×10^{12} from 2.9×10^{12} of the pristine device at $V_g = 60$ V. According to our previous analysis, a reduction in the sheet resistance is of critical importance for enhancing the electron

**ADVANCED
SCIENCE NEWS**

www.advancedsciencenews.com

**ADVANCED
MATERIALS**

www.advmat.de

branch performance. BV doping successfully improved the sheet conductivity of electrons and maintained a low off-current at the same time. Furthermore, the BV dopant is air-stable, giving rise to an $MoTe_2$ device coated with a BV layer that protects the device from the atmospheric O_2 and preserves the performance stability. BV doping presents a good option for modulating the $MoTe_2$ FET properties for use in other complicated functional devices. The carrier transport behaviors in the doped device were confirmed by the temperature dependence of the transfer curves shown in Figure 4d. We plotted the transfer curves over the temperature range 220–300 K. The temperature did not exceed 300 K (room temperature) because the doping concentration varied with the temperature beyond room temperature, which would override the actual temperature dependence of the device (Figure S4b, Supporting Information). The doped $MoTe_2$ device showed almost negligible dependence on the temperature, as compared to the large temperature dependence of the pristine device. The weak temperature dependence may result from tunneling-dominated contact properties because of high electron density induced smaller barrier width. At high positive gate bias, it is also possible that a metallic channel was induced; and thus the current decreases with

increasing temperature, which compensated the positive correlation of current and temperature from weak thermionic emission. The corresponding band diagram of tunneling-dominated contact is shown in the inset of Figure 4d.

$MoTe_2$ FETs suffer from performance degradation due to intrinsic tellurium defects within the $MoTe_2$ flakes. These defects readily absorb oxygen or other impurities from the atmosphere, thereby altering the device properties. We recorded the performances of the as-prepared $MoTe_2$ FET devices and compared these performances with those measured after storing the device in ambient for three months. As shown in **Figure 5**a, the as-prepared $MoTe_2$ FET displayed normal n-dominated ambipolar transfer characteristics. The device displayed p-dominated ambipolar characteristics with a significant reduction in the on–off ratio (about 100) after three months. It became necessary to develop a method for enhancing the stability of the $MoTe_2$ flakes. Al_2O_3 capping has been successfully used in MoS_2 and BP FETs to tune the electric properties and enhance the device stabilities.[2,44,45] The capping layer is usually deposited by atomic layer deposition (ALD). Here, we deposited 30 nm Al_2O_3 onto the $MoTe_2$ flake after device fabrication to measure the performance
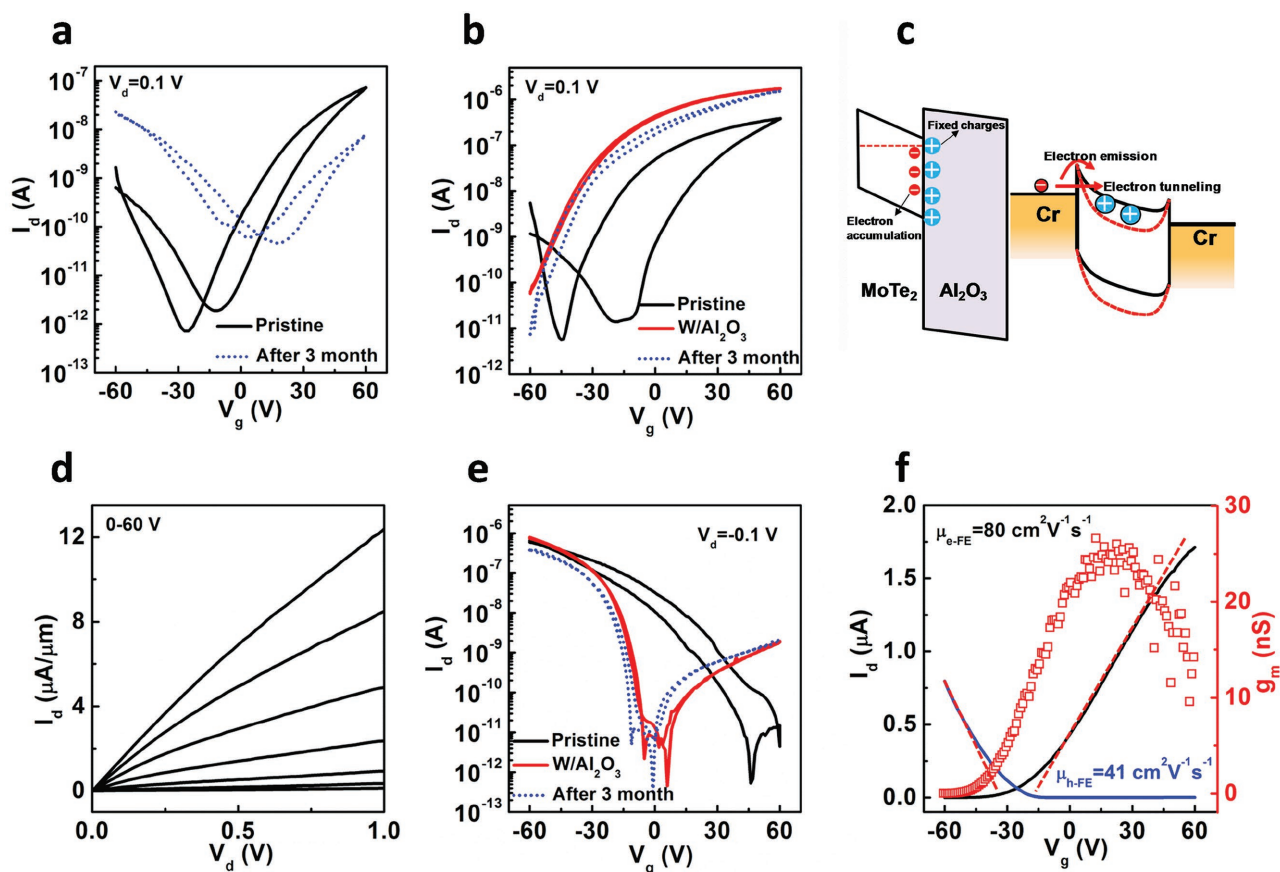

Figure 5. Al_2O_3 capping to enhance the carrier mobility and device stability. a) Performance degradation of an $MoTe_2$ transistor with an exposed surface. b) Effect of Al_2O_3 capping on a pristine ambipolar $MoTe_2$ transistor, and the stability of the capped device. c) The left panel illustrates band bending at the $MoTe_2$-Al_2O_3 interface induced by the positively charged impurities in Al_2O_3. The right panel shows the band diagram of the carrier transport paths in an Al_2O_3-capped $MoTe_2$ transistor. d) Output curves of Al_2O_3 capped n-type $MoTe_2$ transistor. e) Effect of Al_2O_3 capping on a doped unipolar p-type $MoTe_2$ transistor, and the stability of the capped device. f) Electron and hole mobilities extraction from the linear plot of their transfer curves, the red squares is a plot of electron transconductance with respect to gate bias.

**ADVANCED
SCIENCE NEWS**

www.advancedsciencenews.com

**ADVANCED
MATERIALS**

www.advmat.de

differences before and after Al_2O_3 capping. We first tested the device performances of an as-prepared $MoTe_2$ FET (black curve in Figure 5b). The device was then characterized immediately after depositing an Al_2O_3 layer. Interestingly, the transfer characteristic of the capped device changed from a pristine ambipolar state to a unipolar n-type state with an enhanced electron current level. Al_2O_3 capping-induced n-type doping was probably possible due to band bending at the $MoTe_2$–Al_2O_3 interface induced by positive fixed charges in the dielectric layer.[46] The Al_2O_3 layer was deposited at 200 °C.[47] The low-temperature growth process gave rise to positive fixed charges, which induced higher electron concentration at $MoTe_2$–Al_2O_3 interface, leading to reduced effective SBH for electrons. Simultaneously the hole concentration was lowered, and thus the originally weak p-branch cannot be observed any more.[48] Band bending and the corresponding carrier transport paths of the device with Al_2O_3 capping layer are illustrated in Figure 5c. It should be noted that the hysteresis in the capped devices was significantly reduced to be almost indiscernible. Since Al_2O_3 deposition was done at 200 °C, the reduction in hysteresis is probably due to the removal of absorbents from $MoTe_2$ surface during the deposition process.[49] Those absorbents induced trap states within the band gap. Gate induced charged carriers were forced to fill the trap states firstly, and electric conduction can only be realized under relatively high gate voltage.[30] When trap states were removed, gate became more effective and the devices were switched on more rapidly as we observed in Figure 5b,e. Also, electrons induced by the positive charges in Al_2O_3 can fill the trap states, rendering the gate modulation more effective. The stability of the device prepared with or without an Al_2O_3 capping layer was examined by measuring the device performances after storing the capped device under an ambient atmosphere for three months. Unlike the un-capped device, the performance of the device prepared with a 30 nm Al_2O_3 capping layer experienced almost no degradation. Only a very small current reduction could be observed in the transfer curves of the as-capped device (solid red line) and the three-month-stored device (short dot blue line). The output curves of the capped device are shown in Figure 5d. The output curves displayed a trend toward saturation as the drain bias increased, indicating a high electron density has been achieved; and thus the channel resistance is significantly reduced and contact resistance become dominant.

We next deposited a 30 nm Al_2O_3 layer onto a unipolar p-type $MoTe_2$ device obtained by annealing in an RTA at a vacuum level of 8 mTorr, as described previously. The conductivity minimum point of the capped device shifted toward a negative gate bias, and the electron branch rose to a nA current level, as shown in Figure 5e. The transfer characteristics of the capped device were then ambipolar, indicating a certain extent of n-type doping effect upon the annealing doped unipolar p-type device. Although Al_2O_3 capping promoted electron conduction in an annealed unipolar p-type device, hysteresis in the p-branch was reduced, as indicated by the solid red curves in Figure 5e. The on-current level of the holes did not degrade after Al_2O_3 capping. The device performance was preserved after three months storage in an ambient atmosphere (see the short dotted blue line in Figure 5e). The output curves measured after capping are shown in Figure S5 in the

Supporting Information. These curves were more linear and symmetric compared to those obtained from the pristine un-capped unipolar p-type device, showing better contact properties. High-k screening can enhance the carrier mobility in a transistor.[50] The electron and hole field effect mobilities were extracted and shown in Figure 5f. The hole mobility increased to 41 cm^2 V^{-1} s^{-1}, compared to 21 cm^2 V^{-1} s^{-1} obtained from the un-capped device. This is the highest value ever obtained from an $MoTe_2$ transistor on an SiO_2 substrate at room temperature. The electron mobility was further improved to 80 cm^2 V^{-1} s^{-1}, compared to 25 cm^2 V^{-1} s^{-1} obtained from BV doped device. We also plotted the transconductance of capped n-type device with respect to gate bias in Figure 5f. The transconductance reached a maximum value at $V_g = 30$ V and then decreased as the gate voltage was further increased, indicating an even higher electron sheet density in the Al_2O_3-capped $MoTe_2$ transistor, as compared to that of the unipolar n-type device prepared using BV doping. Al_2O_3 capping further improved the n-type $MoTe_2$ transistor performance toward real high-performance devices.

The availability of unipolar n-type as well as p-type $MoTe_2$ FETs permitted fabrication of a lateral p–n junction device on a single $MoTe_2$ flake. The device fabrication process is described in the experiment section. A schematic diagram of the p–n junction device is shown in **Figure 6**a, and an optical microscopy image is shown in the inset of Figure 6b. The exposed device, with electrodes labeled 1 and 2, was designed to be n-type after BV doping, whereas the Al_2O_3 layer masked parts of the 3 and 4 electrodes to maintain the p-type property; Thus, a p–n junction formed between the electrodes 2 and 3. We observed a clear boundary between electrodes 2 and 3, corresponding to the Al_2O_3 layer. We then measured the three devices in series separately. Their transfer characteristics are shown in Figure 6b. The blue curve was obtained from the exposed electrodes 1 and 2, with BV on the surface. This curve revealed clear n-type behavior with an on–off ratio exceeding 10^6. The black line, which indicated p-type transfer characteristics, was measured from electrodes 3 and 4, representing the Al_2O_3-masked device. The red line indicated the transfer curve obtained from the fabricated p–n junction (electrode 2 and 3). The curve typically follows the lower current of the n- and p-branch and reveals the peak current value at the cross-point of the n- and p-branches. In our case, the p–n junction transfer curve displayed p-type behavior; that is, the current decreased as the gate bias increased. These results are discussed further, below. We next examined the diode properties of the lateral p–n junction, as shown in Figure 6c. A rectifying ratio of 10^4 was obtained at a 0-gate bias, confirming the formation of a lateral $MoTe_2$ p–n junction with decent quality. The forward current was found to decrease with increasing positive gate bias. By contrast, the backward current increased with negative gate bias. These results are plotted in Figure 6d at a drain bias of 1.0 V, and they followed the trend observed in the transfer curve of Figure 6b. These results could be explained with the help of the band diagram in the inset. Application of a positive gate bias produced a very high electron conductivity, whereas the hole channel remained quite resistive, which can be confirmed by the low hole current level measured from the transfer curve. The junction barrier ϕ remained relatively low after band alignment. The high resistive p-branch limited the current flow
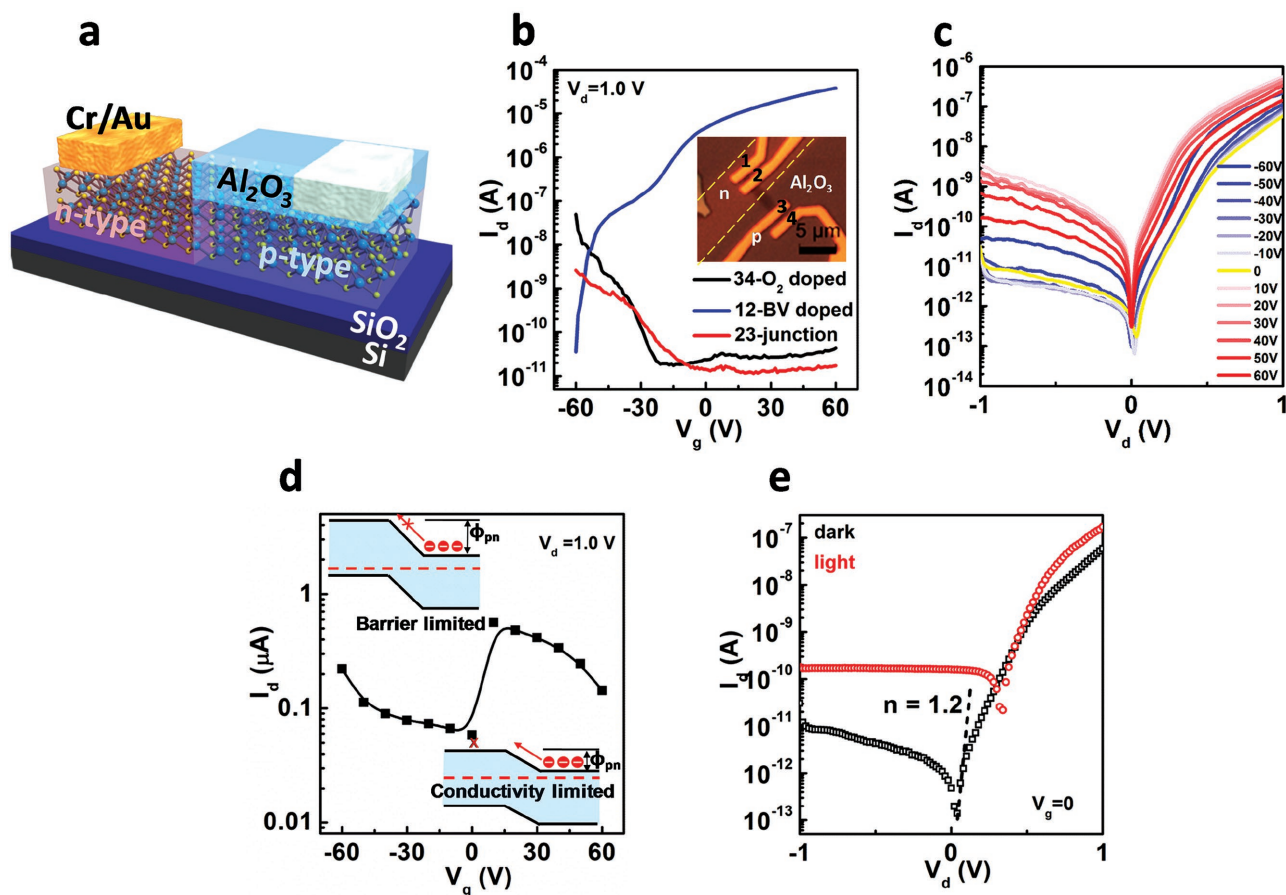
**ADVANCED
SCIENCE NEWS**

www.advancedsciencenews.com

**ADVANCED
MATERIALS**

www.advmat.de

Figure 6. Lateral MoTe$_2$ p–n junction. a) Schematic diagram of a lateral MoTe$_2$ p–n junction device with an Al$_2$O$_3$ mask. b) Transfer curves measured from the n branch, p branch, and the middle p–n junction, respectively, and optical microscopy image of the device shown in the inset. c) Gate tunability of the fabricated MoTe$_2$ p–n diode. d) Forward current variation with the gate bias, and the band diagrams shown in the inset. e) Photoresponse of the p–n diode under incandescent light at a 0-gate bias, from which the ideality factor of this p–n diode in the dark was calculated to be 1.2.

across the device configuration. Application of a higher positive gate bias reduced the conductivity of the p-branch; the total current was then reduced. The electron branch maintained its high conductivity over a wide gate bias range up to −50 V. Even under a negative gate bias, the electron conductivity remained comparable to the hole conductivity. In this case, the carrier flow in the p–n junction was limited by the barrier at the n- and p-type interface, as illustrated by the band diagram in the top left corner of Figure 6d. As the negative gate bias increased, the of the n-branch shifted down; therefore, the junction barrier become lower and lower after band alignment with the p-branch, leading to an increasing trend of current level with increasing negative gate bias. We calculated the ideality factor[51] of the fabricated MoTe$_2$ p–n junction from the dark current at 0-gate bias, which was 1.2, as shown in Figure 6e. This value was very close to 1, a value that can only be obtained in an ideal p–n junction. Clear photoresponse of the fabricated p–n diode was observed when we compare the dark current and current under incandescent light. By combining both p-doping through an annealing process and n-doping through BV coating, our process shows potential for achieving high-quality p–n junction devices.

We developed an RTA process for p-type doping of MoTe$_2$ FETs, in which the doping concentration could be controlled precisely across a wide range simply by varying the vacuum level of the RTA chamber prior to annealing. As a result, the pristine n-dominated ambipolar MoTe$_2$ FET behaviors could be modulated to display symmetric ambipolar, unipolar p-type, or n-type behavior using our doping method. We optimized the n-type MoTe$_2$ FET doping process using BV. The unipolar p- and n-type device performances were further enhanced by Al$_2$O$_3$ capping. The hole and electron mobilities increased to 41 and 80 cm^2 V^{-1} s^{-1}, respectively, upon Al$_2$O$_3$ capping, whereas the device stability was enhanced. The doping methods developed here were used to fabricate a lateral homogeneous MoTe$_2$ p–n junction with a high rectifying ratio of 10^4 and an ideality factor of 1.2, revealing the potential utility of this method for the preparation of future functional devices based on MoTe$_2$.

Experiment Section

MoTe$_2$ FET: Multilayer MoTe$_2$ prepared using the mechanical exfoliation method was positioned on a highly doped p-Si substrate

**ADVANCED
SCIENCE NEWS**

www.advancedsciencenews.com

**ADVANCED
MATERIALS**

www.advmat.de

capped with a 285 nm thermally oxidized SiO_2 layer. A 5/50 nm Cr/Au layer was then deposited onto the $MoTe_2$ flake to form the source and drain contacts using an electron beam evaporator.

XPS Characterization: XPS was conducted with a Thermo Scientific ESCALAB 250 Xi X-ray photoelectron spectrometer with a monochromatic KR Al X-ray line. Core level spectra were collected with a pass energy of 30 eV and a dwell time of 50 ms. All spectra were calibrated using the C 1s peak at 284.6 eV as a reference.

BV Doping: The BV dopant was spread across the device surface by spin coating at 3500 rpm for 1 min. All doping processes were carried out in a glove box to avoid reaction with water or oxygen.

Al_2O_3 Deposition: The Al_2O_3 deposition was carried out over a range of ALD cycle numbers using a trimethylaluminum/water precursor at 200 °C in a custom-built thermal ALD system.

Lateral $MoTe_2$ p-n Junction Fabrication: Four electrodes were first deposited onto the flake to enable separate measurements of the n- and p-branches after doping. The device was then annealed in RTA using the conditions described above to obtain a unipolar p-type transistor. A 30 nm Al_2O_3 layer was deposited to cover the entire flake, followed by polymethyl methacrylate patterning and hydrofluoric (HF) acid etching to expose half of the flake and electrodes. The HF used here was diluted to 1 wt% using deionized water to slow down and accurately control the etching process. A 5×10^{-3} M BV dopant solution was spread onto the device surface by spin coating. The 1×10^{-3} M BV dopant solution used previously on the pristine ambipolar $MoTe_2$ device was not used here to obtain the n side of the p–n junction because the device was doped to p-type beforehand; thus, a high concentration of the n dopant was needed to tune the polarity of the device.

Supporting Information

Supporting Information is available from the Wiley Online Library or from the author.

Acknowledgements

Conflict of Interest

The authors declare no conflict of interest.

Keywords

[1] K. S. Novoselov, A. K. Geim, S. V. Morozov, D. Jiang, Y. Zhang, S. V. Dubonos, I. V. Grigorieva, A. A. Firsov, *Science* **2004**, *306*, 666.

[2] B. Radisavljevic, A. Radenovic, J. Brivio, V. Giacometti, A. Kis, *Nat. Nanotechnol.* **2011**, *6*, 147.

[3] L. Li, Y. Yu, G. J. Ye, Q. Ge, X. Ou, H. Wu, D. Feng, X. H. Chen, Y. Zhang, *Nat. Nanotechnol.* **2014**, *9*, 372.

[4] A. Splendiani, L. Sun, Y. Zhang, T. Li, J. Kim, C. Y. Chim, G. Galli, F. Wang, *Nano Lett.* **2010**, *10*, 1271.

[5] S. Das, J. Appenzeller, *Appl. Phys. Lett.* **2013**, *103*, 103501.

[6] T. Roy, M. Tosun, X. Cao, H. Fang, D. H. Lien, P. Zhao, Y. Z. Chen, Y. L. Chueh, J. Guo, A. Javey, *ACS Nano* **2015**, *9*, 2071.

[7] H. Wang, L. L. Yu, Y. H. Lee, Y. M. Shi, A. Hsu, M. L. Chin, L. J. Li, M. Dubey, J. Kong, T. Palacios, *Nano Lett.* **2012**, *12*, 4674.

[8] H. M. Li, D. Lee, D. Qu, X. Liu, J. Ryu, A. Seabaugh, W. J. Yoo, *Nat. Commun.* **2015**, *6*, 6564.

[9] D. Qu, X. Liu, F. Ahmed, D. Lee, W. J. Yoo, *Nanoscale* **2015**, *7*, 19273.

[10] X. Liu, D. Qu, J. Ryu, F. Ahmed, Z. Yang, D. Lee, W. J. Yoo, *Adv. Mater.* **2016**, *28*, 2345.

[11] W. Liu, J. Kang, D. Sarkar, Y. Khatami, D. Jena, K. Banerjee, *Nano Lett.* **2013**, *13*, 1983.

[12] T. A. Ameen, H. Ilatikhameneh, G. Klimeck, R. Rahman, *Sci. Rep.* **2016**, *6*, 28515.

[13] H. Liu, A. T. Neal, Z. Zhu, Z. Luo, X. Xu, D. Tomanek, P. D. Ye, *ACS Nano* **2014**, *8*, 4033.

[14] D. Xiang, C. Han, J. Wu, S. Zhong, Y. Liu, J. Lin, X. A. Zhang, W. Ping Hu, B. Ozyilmaz, A. H. Neto, A. T. Wee, W. Chen, *Nat. Commun.* **2015**, *6*, 6485.

[15] D. Yue, D. Lee, Y. D. Jang, M. S. Choi, H. J. Nam, D. Y. Jung, W. J. Yoo, *Nanoscale* **2016**, *8*, 12773.

[16] D. J. Perello, S. H. Chae, S. Song, Y. H. Lee, *Nat. Commun.* **2015**, *6*, 7809.

[17] Y. F. Lin, Y. Xu, S. T. Wang, S. L. Li, M. Yamamoto, A. Aparecido-Ferreira, W. W. Li, H. B. Sun, S. Nakaharai, W. B. Jian, K. Tsukagoshi, *Adv. Mater.* **2014**, *26*, 3263.

[18] I. G. Lezama, A. Ubaldini, M. Longobardi, E. Giannini, C. Renner, A. B. Kuzmenko, A. F. Morpurgo, *2D Mater.* **2014**, *1*, 021002.

[19] C. Ruppert, O. B. Aslan, T. F. Heinz, *Nano Lett.* **2014**, *14*, 6231.

[20] I. G. Lezama, A. Arora, A. Ubaldini, C. Barreteau, E. Giannini, M. Potemski, A. F. Morpurgo, *Nano Lett.* **2015**, *15*, 2336.

[21] S. Nakaharai, M. Yamamoto, K. Ueno, K. Tsukagoshi, *ACS Appl. Mater. Interfaces* **2016**, *8*, 14732.

[22] Y. F. Lin, Y. Xu, S. T. Wang, S. L. Li, M. Yamamoto, A. Aparecido-Ferreira, W. Li, H. Sun, S. Nakaharai, W. B. Jian, K. Ueno, K. Tsukagoshi, *Adv. Mater.* **2014**, *26*, 3263.

[23] Y. Guo, D. Liu, J. Robertson, *Appl. Phys. Lett.* **2015**, *106*, 173106.

[24] C. Gong, L. Colombo, R. M. Wallace, K. Cho, *Nano Lett.* **2014**, *14*, 1714.

[25] L. Li, M. Engel, D. B. Farmer, S. J. Han, H. S. Wong, *ACS Nano* **2016**, *10*, 4672.

[26] N. R. Pradhan, D. Rhodes, S. M. Feng, Y. Xin, S. Memaran, B. H. Moon, H. Terrones, M. Terrones, L. Balicas, *ACS Nano* **2014**, *8*, 5911.

[27] N. Haratipour, S. J. Koester, presented at *72nd Annual Device Research Conference (DRC)*, Santa Barbara, CA, USA, June **2014**.

[28] H. L. Xu, S. Fathipour, E. W. Kinder, A. C. Seabaugh, S. K. Fullerton-Shirey, *ACS Nano* **2015**, *9*, 4900.

[29] Y. Zhang, J. Ye, Y. Matsuhashi, Y. Iwasa, *Nano Lett.* **2012**, *12*, 1136.

[30] D. Braga, I. Gutierrez Lezama, H. Berger, A. F. Morpurgo, *Nano Lett.* **2012**, *12*, 5218.

[31] G. Nazir, M. F. Khan, V. M. Iermolenko, J. Eom, *RSC Adv.* **2016**, *6*, 60787.

[32] M. S. Kang, C. D. Frisbie, *ChemPhysChem* **2013**, *14*, 1547.

[33] B. Radisavljevic, A. Kis, *Nat. Mater.* **2013**, *12*, 815.

[34] K. Choi, Y. T. Lee, J. S. Kim, S. W. Min, Y. Cho, A. Pezeshki, D. K. Hwang, S. Im, *Adv. Funct. Mater.* **2016**, *26*, 3146.

[35] J. Heo, H. Jeong, Y. Cho, J. Lee, K. Lee, S. Nam, E. K. Lee, S. Lee, H. Lee, S. Hwang, S. Park, *Nano Lett.* **2016**, *16*, 6746.

[36] H. S. Liu, N. N. Han, J. J. Zhao, *RSC Adv.* **2015**, *5*, 17572.

[37] B. Chen, H. Sahin, A. Suslu, L. Ding, M. I. Bertoni, F. M. Peeters, S. Tongay, *ACS Nano* **2015**, *9*, 5326.

[38] L. Yang, K. Majumdar, H. Liu, Y. Du, H. Wu, M. Hatzistergos, P. Y. Hung, R. Tieckelmann, W. Tsai, C. Hobbs, P. D. Ye, *Nano Lett.* **2014**, *14*, 6275.

[39] J. D. Lin, C. Han, F. Wang, R. Wang, D. Xiang, S. Qin, X.-A. Zhang, L. Wang, H. Zhang, A. T. S. Wee, *ACS Nano* **2014**, *8*, 5323.

[40] A. Nipane, D. Karmakar, N. Kaushik, S. Karande, S. Lodha, *ACS Nano* **2016**, *10*, 2128.

[41] B. Chen, H. Sahin, A. Suslu, L. Ding, M. I. Bertoni, F. Peeters, S. Tongay, *ACS Nano* **2015**, *9*, 5326.

[42] D. Kiriya, M. Tosun, P. D. Zhao, J. S. Kang, A. Javey, *J. Am. Chem. Soc.* **2014**, *136*, 7853.

[43] M. K. Chen, H. Nam, S. J. Wi, L. Ji, X. Ren, L. F. Bian, S. L. Lu, X. G. Liang, *Appl. Phys. Lett.* **2013**, *103*, 142110.

[44] H. Liu, D. Y. Peide, *IEEE Electron Device Lett.* **2012**, *33*, 546.

[45] J. D. Wood, S. A. Wells, D. Jariwala, K. S. Chen, E. Cho, V. K. Sangwan, X. Liu, L. J. Lauhon, T. J. Marks, M. C. Hersam, *Nano Lett.* **2014**, *14*, 6964.

[46] H. Liu, A. T. Neal, M. W. Si, Y. C. Du, P. D. Ye, *IEEE Electron Device Lett.* **2014**, *35*, 795.

[47] J. Yang, S. Kim, W. Choi, S. H. Park, Y. Jung, M. H. Cho, H. Kim, *ACS Appl. Mater. Interfaces* **2013**, *5*, 4739.

[48] J. Buckley, B. De Salvo, D. Deleruyelle, M. Gely, G. Nicotra, S. Lombardo, J. F. Damlencourt, P. Hollinger, F. Martin, S. Deleonibus, *Microelectron. Eng.* **2005**, *80*, 210.

[49] S. D. Namgung, S. Yang, K. Park, A. J. Cho, H. Kim, J. Y. Kwon, *Nanoscale Res. Lett.* **2015**, *10*, 62.

[50] X. Liu, E. H. Hwang, W. J. Yoo, S. Lee, B. K. Cheong, *Solid State Commun.* **2015**, *209*, 1.

[51] M. S. Choi, D. Qu, D. Lee, X. Liu, K. Watanabe, T. Taniguchi, W. J. Yoo, *ACS Nano* **2014**, *8*, 9332.